International Journal of Nanomedicine

Dovepress
Taylor & Francis Group

Open Access Full Text Article

ORIGINAL RESEARCH

Self-Assembled Carrier Free Oligomeric Proanthocyanidin/Tetrandrine Nanoparticles Ameliorate Osteoarthritis via Anti-Inflammatory and Anti-Ferroptotic Pathways

Chengyuan Xing[1,*], Yu Wu[1,*], Yao Huang[1], Weijie Li[1], Xie Wang[2], Huikun Chen[1]

[1]Institute of Sports Medicine and Health, Sports Medicine Key Laboratory of Sichuan Province, Key Laboratory of Sports Medicine, General Administration of Sport of China, Chengdu Sport University, Chengdu, Sichuan, People's Republic of China; [2]Department of Anesthesiology, Sichuan Provincial People's Hospital, School of Medicine, University of Electronic Science and Technology of China, Chengdu, Sichuan, People's Republic of China

*These authors contributed equally to this work

Correspondence: Xie Wang; Huikun Chen, Email wangxiemz@med.uestc.edu.cn; huikunchen97@gmail.com

Purpose: This study aims to design and characterize Oligomeric Proanthocyanidin-Tetrandrine nanoparticles (OPC-Tet NPs) in alleviating progress of osteoarthritis (OA) by anti-inflammatory and anti-ferroptosis mechanism.

Methods: A carrier-free drug delivery system (DDS) has been designed based on OPC and Tet with the unification of medicines and excipients. In vitro studies have evaluated biosafety, cellular internalization, suppression of oxidative stress, and maintaining iron homeostasis in RAW 264.7 cells. The treatment efficacy and mechanism were investigated by using the papain-induced OA mouse model.

Results: OPC and Tet were successfully self-assembled into NPs with a particle size of 153 nm approximately, exhibiting a spherical morphology, and narrow size distribution. In vitro results indicated that OPC-Tet NPs exhibit good biocompatibility with 78.4% cell viability at a concentration of 40 μg/mL. The results from micro-CT and pathological staining demonstrate that OPC-Tet NPs can effectively improve bone volume fraction (BV/TV [%]) by 30.5% compared to model group ($P < 0.001$). Furthermore, IHC experiments showed that OPC-Tet NPs could mediate inflammation and ferroptosis to manage OA.

Conclusion: In summary, our results demonstrate OPC-Tet NPs show good biocompatibility, and treatment effect. The treatment mechanism of anti-inflammation and anti-ferroptosis were also verified. The current research not only offers a new strategy to manage OA but also provides more possibilities for potential application of natural products.

Keywords: osteoarthritis, natural products, oligomeric proanthocyanidins, self-assembly, carrier free nanoparticles, ferroptosis

Introduction

During aging, abnormal iron accumulation in organs increases oxidative stress, leading to ferroptosis.[1] Research has shown that OA patient samples exhibit reduced GPX4 activity and expression, elevated lipid peroxides, and increased ferrous iron. Additionally, the upregulation of ACSL4 promotes pro-ferroptotic lipid synthesis. Meanwhile, iron triggers the production of reactive oxygen species (ROS), mitochondrial damage, and lipid peroxidation. Moreover, pro-inflammatory cytokines TNF-α and IL-1β upregulate transferrin receptors, thereby enhancing iron uptake.[2,3] Critically ferroptosis releases IL-1β, activating NF-κB to downregulate GPX4, worsening ferroptosis. Ferroptotic cells release injury-related molecular patterns, triggering inflammation. This process is closely related to the occurrence of OA.

According to WHO data in 2019, 528 million individuals worldwide suffer from symptomatic OA.[4] Clinical OA treatment generally involves non-steroidal anti-inflammatory drugs (NSAIDs), hyaluronic acid injections, and joint replacement surgeries, primarily alleviate symptoms without halting cartilage degradation.[5] Therefore, more effective

Received: 2 April 2025
Accepted: 13 October 2025
Published: 30 October 2025

Graphical Abstract

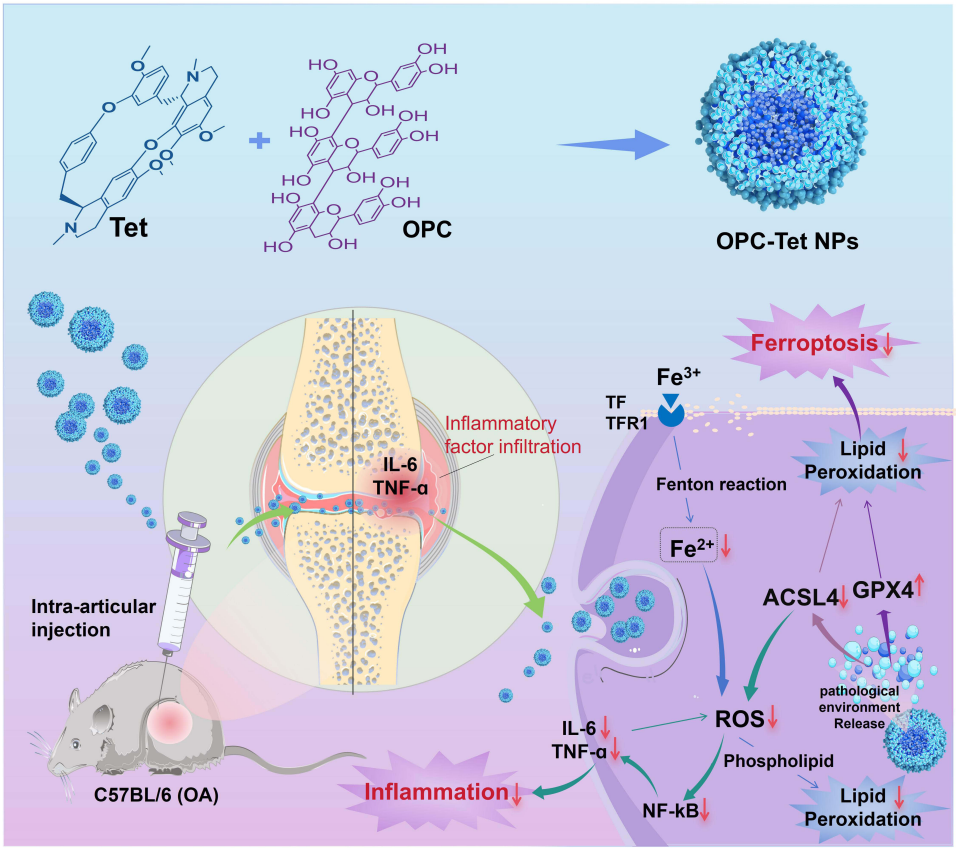

treatment strategy should be considered. Ferroptosis inhibitors such as liproxstatin-1, deferoxamine have shown promising results in OA models in recent years. However, multi-targeting therapeutics may get much benefit from OA treatment. The effective components derived from traditional Chinese medicine have provided an effective solution to this problem.

Tet, a major bioactive component derived from the Chinese herbal medicine *Radix Stephaniae tetrandrae*, possess excellent anti-inflammatory and anti-ferroptosis abilities and is widely recommended for treating OA in "Guidelines for the diagnosis and treatment of osteoarthritis in China (2024 edition)".[6–8] However, the clinical application of Tet is primarily limited by its low bioavailability and poor pharmacokinetic profile affecting Tet's efficacy. Enhancing the bioavailability of Tet stands as a key step for actualizing its potential.

In recent years, research on DDS has gained widespread attention. Studies use excipients to enhance drug solubility and improve bioavailability, showing potential for increasing the clinical value of Tet.[9] However, the safety profile of excipients remains uncertain.[10] It has been reported that natural products possess good biocompatibility, including low cytotoxicity and tissue accumulation. Additionally, research reported that natural products possess the ability to self-assembly via complex interactions. Natural product-derived therapeutics thus represent promising OA treatment strategies.[11]

OPC, natural condensed tannins, and their derivatives—including Sophora alkaloids tannate capsules and berberine tannate-enhance drug solubility and bioavailability. Notably, OPC has shown significant efficacy in treating OA based on anti-ferroptosis mechanism according to literature.[12,13] Based on the biochemical properties of OPC, it is possible to design a DDS with unification of medicines and excipients. Carrier-free nanodrugs have demonstrated superior efficiency

for drug delivery, featuring 100% drug loading, synergistic therapeutic enhancement, and minimal systemic toxicity.[14] However, self-assembly by two small molecules (Mw < 500) may face stability problem of the prepared nanodrugs.[15] The introduction of a molecule with high molecular weight such as OPC could mitigate this problem. Therefore, Tet and OPC, as two natural products, are expected to become a nanomedicine for managing OA without additional excipients.

Here, OPC and Tet were successfully self-assembled into NPs with a particle size of 153 nm, exhibiting a spherical morphology, narrow size distribution, and remarkable stability in aqueous solution. The biocompatibility of OPC-Tet NPs has been confirmed through in vitro and in vivo studies. In this context, the therapeutic efficacy of OPC-Tet NPs has been confirmed by micro-CT and pathological staining. Moreover, we found that OPC-Tet NPs can mediate inflammation and ferroptosis to manage OA. This research not only offers new strategies for OA management but also proposes a novel perspective on clinical translation of natural products.

Materials and Methods

Reagents and Materials

All reagents used in this study were commercially available. OPC, Tet, Coumarin 6 (C6), papain, and 1, 1-dioctadecyl-3, 3, 3, 3-tetramethylindotricarbocyanine iodide (DIR) were purchased from Zhengzhou Alpha Chemical Co., Ltd. (Zhengzhou, China). Dimethyl sulfoxide (DMSO) was obtained from Chengdu Kelong Chemical Co., Ltd. (Chengdu, China). Lipopolysaccharide (LPS) and paraformaldehyde were purchased from Sigma-Aldrich Co., Ltd., (Shanghai, China). Cell Counting Kit-8 (CCK8) Assay, Live-Dead Viability Kit, Annexin V-FITC/PI Apoptosis Detection Kit, FerroOrange (Fe^{2+} indicator) ferrous ion fluorescent probe, Malondialdehyde (MDA) Assay kit, Hematoxylin and Eosin (H&E), Saffranin O-Fast Green (SO&FG) Kit Assay, Sirius Red Kit Assay, Toluidine Blue Kit Assay, and Transferase-mediated Nick Labeling (TUNEL) Kit Assay were purchased from Beyotime Biotech. Inc., (Shanghai, China). Anti-IL6 antibody, Anti-TNF-α antibody, Anti-GPX4 antibody and Anti-ACSL4 antibody were purchased from Proteintech Group, Inc. (Wuhan, China). C57BL/6 mice were purchased from SPF Biotechnology Co., Ltd. (Beijing, China).

Preparation of OPC-Tet NPs

In a low-light environment at 25 °C, 1 mL of OPC (5 mg/mL) was added to 15 mL of deionized water. Subsequently, 125 μL of Tet (10 mg/mL) was added dropwise while stirring the mixture with a speed of 600 rpm. The mixture was then sealed and immediately immersed in an ultrasonic water bath for 5 min. The as-prepared NPs were dialysised in a dialysis bag (3500 MWCO) for 12 h to obtain the resultant OPC-Tet NPs.

Characterization of OPC-Tet NPs

The particle size and zeta potential of OPC-Tet NPs were measured at 25 °C using a Zetasizer Nano-ZS90 (Malvern Panalytical, UK). The morphology of the NPs was recorded using a transmission electron microscope (TEM, JEOL, Japan). Ultraviolet-Vis (UV-vis) and fluorescence spectrophotometry (HITACHI, f-7000) were employed to study changes in the photophysical properties of OPC and Tet in OPC-Tet NPs. The formation mechanism of the prepared NPs was characterized by 2D NOESY (solvent: DMSO, Bruker, USA) and Fourier transform infrared spectroscopy (FTIR, Hitachi UH5300, Japan) with a frequency range of 400–4000 cm^{-1}. The molecular dynamics simulation (MD) was performed by GROMACS 2019.6 software to reveal the self-assembly process of OPC-Tet NPs. The Dmol3 module of Materials Studio was employed, with calculations based on the GGA-PBE functional and performed at the software's default fine accuracy level. The core treatment adopted the All-Electron approach, paired with the DNP basis set. The SCF tolerance was set to 1×10^{-6} eV/atom, and the DIIS size was 6. Initially, the structure was optimized; subsequently, based on the optimized structure, further charge analysis was conducted on the molecules to acquire information regarding their electrostatic potential distribution.

Stability of OPC-Tet NPs

The stability of OPC-Tet NPs was assessed over a period of seven days, with daily monitoring of size distribution using dynamic light scattering (DLS).

Release Properties in vitro

The concentration of Tet was analyzed using high-performance liquid chromatography (HPLC, Agilent, Beijing, China). The chromatographic system utilized a Diamonsil TM-C18 stationary phase (4.6 mm × 150 mm, 5 μm) for analyte separation. The mobile phase consisted of a ternary mixture of 0.05 mol/L potassium dihydrogen phosphate solution (pH 3.2), methanol, and acetonitrile (80:30:0.3, v/v/v), and was pumped through the column at a flow rate of 1.0 mL/min. The eluate was monitored at a wavelength of 282 nm. The encapsulation efficiency (EE) of OPC-Tet NPs was calculated using the equation: EE (%) = (W_T - W_F)/W_T × 100%, where W_T is the initial mass of Tet, and W_F is the mass of free Tet in the solution after dialysis. The EE of Tet was 49.4%.

7 mg of OPC-Tet NPs were dissolved in PBS to form a dispersion of drug-loaded particles, which was then placed into an end-capped dialysis membrane submerged in a 50 mL centrifuge tube containing 10 mL of release medium. Drug release from OPC-Tet NPs was investigated at two different pH values (7.4 and 6.8). This setup was placed vertically in a thermostatic shaker set at 25 °C and 180 rpm, shielded from light. Samples were collected at intervals of 0, 3, 6, 9, 12, 24, 36, 48, and 72 h. The resultant supernatants were eventually analyzed using HPLC. The drug loading content (DLC) of OPC-Tet NPs was calculated according to the following equation: DLC (%) = (W_T - W_F)/W_{NPs} × 100%, where W_T is the initial mass of Tet, W_F is the mass of free Tet in the solution after ultrafiltration, and W_{NPs} is the mass of the obtained OPC-Tet NPs. The DLC of Tet was 12.3%.

Cell Culture

RAW264.7 cells (Procell Life Science & Technology, China) were cultured in DMEM supplemented with 10% fetal bovine serum (Pansera ES, Germany) and 1% penicillin/streptomycin (Thermo Fisher Scientific, USA). Cells were incubated at 37 °C in a 5% CO_2.

In vitro Cytotoxicity Assay

The cytotoxicity of OPC-Tet NPs on RAW264.7 cells was evaluated using the CCK-8 Assay. RAW264.7 cells were plated in 96-well plates at a seeding density of 5000 cells per well. Subsequently, varying concentrations of OPC-Tet NPs (0, 0.5, 1, 2.5, 5, 10, and 40 μg/mL, refer to Tet) were added to the wells to be tested for 24 h at 37°C. After incubation, the medium was discarded, and 100 μL of a basic medium and CCK-8 mixture (CCK-8 content < 10%) was added to each well. After incubation for 3 h in the dark, the absorbance at 450 nm was determined using a microplate reader. Cell viability was calculated using the formula: Cell viability (%) = [OD_{test} - $OD_{control}$)/(OD_{neg} - $OD_{control}$)] × 100%, where OD_{test} was the absorbance of experimental groups, and OD_{neg} and $OD_{control}$ represent the model and control groups, correspondingly.

Apoptosis Analysis

RAW264.7 cells were seeded in 96-well plates at a density of 1.5×10^5 cells per well. After stimulation with LPS (1.0 μg/mL) for 8 h, the cell culture mediums were replaced with 0.6 μg/mL tetrandrine equivalent for 22 h. Cells were collected and washed twice with pre-cooled PBS. Cells were detached using trypsin without EDTA. The cells were gently resuspended in 195 μL of binding buffer. Sequentially, 5 μL of Annexin V-FITC and 10 μL of PI were added, and cells were incubated for 20 min at 25 °C in a 5% CO_2 incubator, protected from light. The analysis was conducted using flow cytometry (FCM).

Hemolysis Test

Purified red blood cells were centrifuged at 3000 rpm for 15 min. 1 mL of OPC-Tet NPs (0, 0.5, 1, 2.5, 5, 10, and 40 μg/mL), and 1 mL of PBS were mixed with 20 μL of red blood cells. The mixture was incubated at 37 °C for 4 h, then centrifuged again at 3000 rpm for 5 min to assess hemolysis. The absorbance of the supernatant was measured at 542 nm using a microplate reader, with three replicates per group. Hemolysis ratio (%) = [OD_{test} - OD_{PBS})/(OD_{H2O} - OD_{PBS})] × 100%.

Live-Dead Cell Staining

The 1× assay buffer was prepared by diluting the 10× buffer with deionized water and preheating to 37 °C before use. 5 μL of Calcein AM and 1 μL of PI were added to each 1 mL of 1× assay buffer. The cells were washed with PBS (2–3 times), followed by centrifuging for 5 min. The cells were harvested and transferred to a 24-well cell culture plate. Each well was then treated with 0.5 mL of Calcein AM/PI solution and incubated at 37 °C for 30 min in the dark. Finally, the cells were washed twice with PBS. Next, a 490 ± 10 nm excitation filter was used to observe live and dead cells with an inverted fluorescence microscope. The imaging channels included Calcein AM (excitation at 494 nm, emission at 517 nm) and PI (excitation at 535 nm, emission at 617 nm).

In vitro Cellular Uptake Assay

The uptake of OPC-Tet NPs by RAW264.7 cells was assessed using FCM (CytoFLEX, Beckman Coulter, China) with 1 μg/mL C6 equivalent as the fluorescent marker for OPC-Tet NPs, referred to as C6@NPs. Cells were treated with C6@NPs for 0, 1, 3, and 6 h, respectively. After incubation, the cells were washed three times with PBS at 4 °C. Quantitative analysis of cellular uptake was performed on C6-positive cells by FCM.

ROS Assay

RAW264.7 cells were cultured in the presence of 1 μg/mL LPS to simulate an inflammatory environment for 12 h. After which they were transferred to 1 mL of fresh DMEM with 0.6 μg/mL Tet equivalent for 8 h. The cells were incubated with 1 μg/mL DCFH-DA in serum-free medium at 37 °C for 30 min. Finally, ROS generation was detected using FCM and inverted fluorescence microscopy.

Intracellular Fe^{2+} Detection

The cells were washed three times with PBS and then incubated with 5 μL FerroOrange fluorescence probe at 37 °C for 30 min after the culture medium was removed. Fluorescence images were captured using confocal laser scanning microscopy (CLSM). Excitation at 543 nm and emission at 580 nm. Analysis of Fe^{2+} content was conducted by measuring fluorescence intensity for each treatment.

Retention Capability of OPC-Tet NPs in the Knee Joint ex vivo

The OA mice were divided into two groups, one group received intra-articular injections with free DIR (0, 12, 24, and 48 h) and the other group received intra-articular injections with the complex of DIR and OPC-Tet NPs (DIR@NPs, 0, 12, 24, and 48 h). They were photographed on a camera obscura platform (excitation at 748 nm, emission at 780 nm) with a small animal optical imaging system (IVIS Lumina III, USA). The experiment was conducted thrice.

Animal Experiments

All animal experiments complied with the Chinese guidelines for the Ethical Review of Welfare of Laboratory Animals (GB/T 35892–2018) and the Animal Ethics and Welfare Committee of Chengdu Sport University (Approval No. CDSU [2024] No. 46). Mice were kept in standard lab conditions (25°C, 60% humidity, 12h light/dark cycle) with free access to food and water. To reduce variability, animals were individually numbered and randomized via a random number table for group assignment. Eight-week-old C57BL/6 female mice were randomly divided into five groups: control, OA, OPC, Tet, and OPC-Tet NPs, with 6 mice per group. Except for the control group, mice received intra-articular injections of 4% papain (5 μL, 8 μg/kg) every three days for a total of three injections. Mice were excluded with absence of redness or swelling. After 4-weeks of feeding, the mice received intra-articular injections every three days for a total of ten injections. Except the control and OA groups, which received 20 μL of normal saline, OPC group (intra-articular injection of 3.6 mg/kg OPC), Tet group (intra-articular injection of 0.5 mg/kg Tet), OPC-Tet NPs group (intra-articular injection of 4.1 mg/kg BBR-OPAs NPs) received injections every 3-day for 4 weeks.

Micro-CT

After the mice were sacrificed, the intact knee joints were preserved, placed in a 5 mL centrifuge tube and fixed with paraformaldehyde. Micro-CT was performed on the samples using Micro-CT Skyscan 1276 system (Bruker, Kontich, Belgium). Data was analyzed using the manufacturer's testing software. Reconstruction was performed using NRecon (version 1.7.4.2). 3D images were obtained from contoured 2D images based on the distance changes of the grayscale original images using (CTvox; version 3.3.0). Bone morphology measurements were performed on the cortical bone and epiphyseal trabeculae of the femur and tibia using CT Analyzer software (version 1.18.8.0). Parameters measured included bone volume fraction (BV/TV [%]), bone volume (BV [mm^3]), bone surface area (BS [mm^2]), bone surface density (BS/TV [mm^{-1}]), bone surface / volume ratio (BS/BV [mm^{-1}]), trabecular number (Tb. N [mm^{-1}]), trabecular spacing (Tb. Sp [mm]), trabecular mode factor (Tb. Pf [mm^{-1}]), and bone mineral density (BMD [g. cm^{-3}]).

Histopathology

Mice tissues were fixed in 4% paraformaldehyde for 24 h. Follow fixation, tissues were dehydrated through a series of graded ethanol solutions, cleared in xylene, and embedded with paraffin. After dewaxing and dehydration, the sections (5 μm) were stained with H&E, SO&FG, Sirius Red and Toluidine Blue. Images were captured and analyzed using a microscopy (DM6B, Leica, Germany). The Knee joint injury was evaluated using the modified Mankin histological scoring system, with a score ranging from 0 (normal tissue) to 12 (complete tissue loss and cell proliferation). We also evaluated the treatment of OPC-Tet NPs using the osteoarthritis bone score OABS system in OA.

IHC and Immunofluorescence (IF) Analysis

Sagittal slices (5 μm) were obtained and deparaffinized in deionized water. Antigen retrieval was performed by boiling in sodium citrate buffer. Sections were then blocked with fetal bovine serum (FBS) for 1 h. Primary antibodies (1: 400 for anti-IL-6, 1: 300 for anti-TNF-α, and 1: 200 for anti-GPX4, 1: 300 for anti-ACSL4) were incubated overnight at 4 °C in a humidified environment. The HRP-conjugated secondary antibody was applied to detect the primary antibody for 30 min on day 2. Finally, the 3, 3′-diaminobenzidine (DAB) was used for coloration. Images were captured using a microscope.

To further verify the anti-inflammatory effects of OPC-Tet NPs, IF was used to quantify IL-6 and TNF-α. After incubating the slices with the primary antibody (1: 200 for anti-IL-6 and 1: 300 for anti-TNF-α), add the fluorescent secondary antibody dilution and then incubate in the dark at 25 °C for 1 h. Then, the DAPI (1: 1000) was added, diluted, and incubated at room temperature for 1 min before mounting the slides. Finally, images were captured using a confocal laser scanning microscope.

A TUNEL staining was also conducted. Briefly, paraffin sections were heated at 60 °C for 20 min to improve adhesion. Sections were then dewaxed with xylene and hydrated through a graded ethanol series. Following rehydration, sections were incubated proteinase K at 25 °C for 30 min, followed by incubating with TUNEL staining solution at 25 °C in a humidified chamber for 60 min. DAB staining was performed at 25 °C for 10 min, and re-stained with hematoxylin. Finally, sections cleared in xylene and sealed.

Statistical Analysis

The statistical analysis was performed using GraphPad Prism 10.0 (GraphPad Prism software, San Diego, CA, USA). The results represent the mean ± standard error of the mean from triplicate measurements. One-way ANOVA was employed to assess the differences between each group, with significance determined by a P-value less than 0.05.

Results and Discussion

Characterization of NPs

OPC-Tet NPs were successfully synthesized, as detailed in Figure 1A. The particle size of OPC-Tet NPs was 153 ± 15 nm (Figure 1B), and the zeta potential was −17.4 ± 4.8 mV (Figure 1C). Under TEM, a clear boundary of the OPC-Tet NPs was visible, with a low-density shadow at the edge (Figure 1D). The stability of OPC-Tet NPs was verified by measuring the particle size over seven days, showing no noticeable changes (Figure 1E), indicating the system was stable.

Since the pH value of synovia from OA could be below 6.8, the drug release was studied at both pH 7.4 and pH 6.8.[16] After dialyzing NPs in various pH environments (7.4 and 6.8) at 37 °C, approximately 15% and 57% of Tet were released. NPs exhibited different release rates at varying pH levels, suggesting that pH influences NPs stability. Mathematical models were employed to analyze drug release mechanisms quantitatively. The release kinetic data was fitted using the Ritger-Peppas model, providing insights into the drug release mechanism of OPC-Tet NPs. The influence of pH was measured using constant k: if k is less than 0.45, release occurs via Fickian diffusion; between 0.45 and 0.89, via anomalous transport; above 0.89, via skeletal corrosion. As shown in Figure 1F and Table S1, the release mechanism of OPC-Tet NPs followed anomalous transport in pH = 7.4 and skeletal corrosion primarily in pH = 6.8.[17]

The Self-Assembly of NPs

2D-NOESY spectroscopy was employed to elucidate the non-covalent interactions between OPC and Tet (Figure 2A). Based on the 2D-NOESY spectrum, the binding mode between OPC and Tet was analyzed. Several cross-peaks (6.6–6.9 ppm and 6.4–6.5 ppm) attributed to the aromatic ring interactions indicated the presence of π-π interactions. Considering the characteristic peaks of OPC at 6–7 ppm, it is suggested that OPC and Tet exhibit π-π interactions. Strong NOE cross-

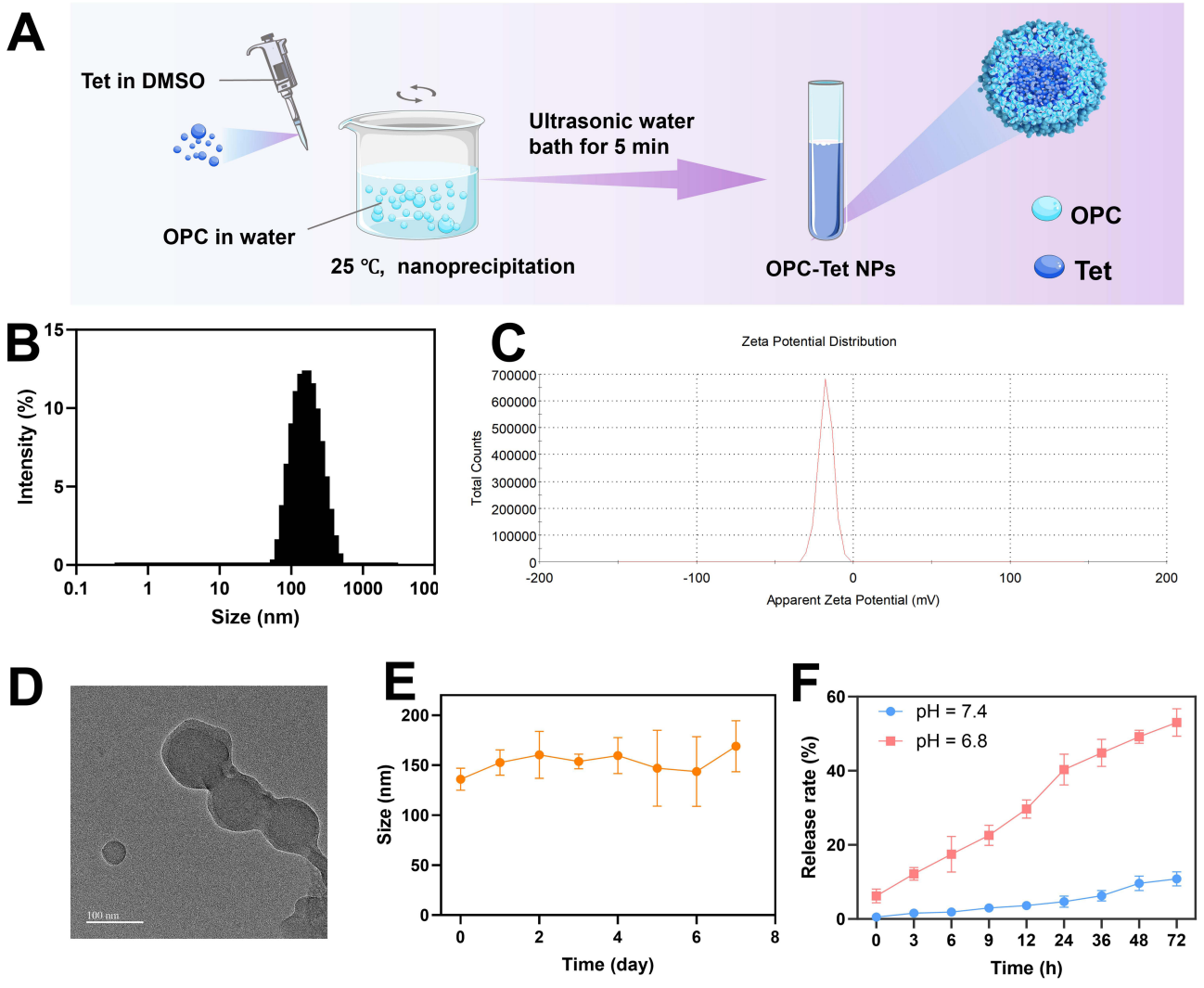

Figure 1 Characterization of the as-prepared OPC-Tet NPs. (**A**) Schematic illustration of the preparation of OPC-Tet NPs. (**B**) Diameter of OPC-Tet NPs. The mean diameter of the as-prepared NPs was 153 ± 15 nm; (**C**) Zeta potential of OPC-Tet NPs. The mean zeta potential of the as-prepared NPs was −17.4 ± 4.8 mV; (**D**) The morphology of OPC-Tet NPs characterized by TEM. (**E**) Stability of the as-prepared OPC-Tet NPs in water. (**F**) In vitro Tet release rate from OPC-Tet NPs in various pH environments (7.4 and 6.8). Mean ± SD, n = 3.

https://doi.org/10.2147/IJN.S531873

peaks were observed between the CH from OPC and the CH_2 from Tet, indicating that OPC and Tet were close in space. In the spectrum, strong interactions between OPC and Tet were observed.[18,19]

The photophysical properties of OPC, Tet, and OPC-Tet NPs were tested using UV-vis and fluorescence spectroscopy (Figure 2B and C). The fluorescence spectra showed that Tet and OPC-Tet NPs have the same characteristic peak, indicating the presence of Tet within them. OPC-Tet NPs exhibited a new peak at 467 nm, demonstrating the interaction between OPC and Tet. In the UV-vis spectrum, OPC displayed peaks at 214 and 279 nm, and OPC-Tet NPs also showed these peaks, confirming the presence of OPC. Since Tet did not have a significant absorption peak, the appearance of new peaks in the NPs spectra further indicates an interaction between OPC and Tet.

FTIR analysis also revealed the characteristic bands between OPC and Tet (Figure 2D). For OPC, there was a wide absorption signal at ~3350 cm^{-1}, which indicated the overlap of the -OH groups of OPC, demonstrating the presence of strong hydrogen bonds. In addition, 1264 and 1106 cm^{-1} were stretching vibrations of C-O and C-O-C, respectively. There were strong absorption peaks for 1601, 1567, and 1500 cm^{-1} of Tet, which were the absorption peak of stretching vibration of benzene ring skeleton, and 2937 cm^{-1} was the characteristic absorption peak of $-OCH_3$. 1031 cm^{-1} was the absorption peak of C-O-C stretching vibrations. After self-assembly, a wide O-H bending vibration peak was exhibited at 3350 cm^{-1}, the C-O-C stretching vibration peak was red shifted, and the aromatic ring skeleton in the system was slightly blue-shifted relative to Tet.

The self-assembly process of OPC and Tet was further analyzed by MD. Figure 2E showed the aggregation of OPC and Tet and the possible molecular stacking status. The OPC-Tet NPs self-assembled to form a nanocluster structure. We

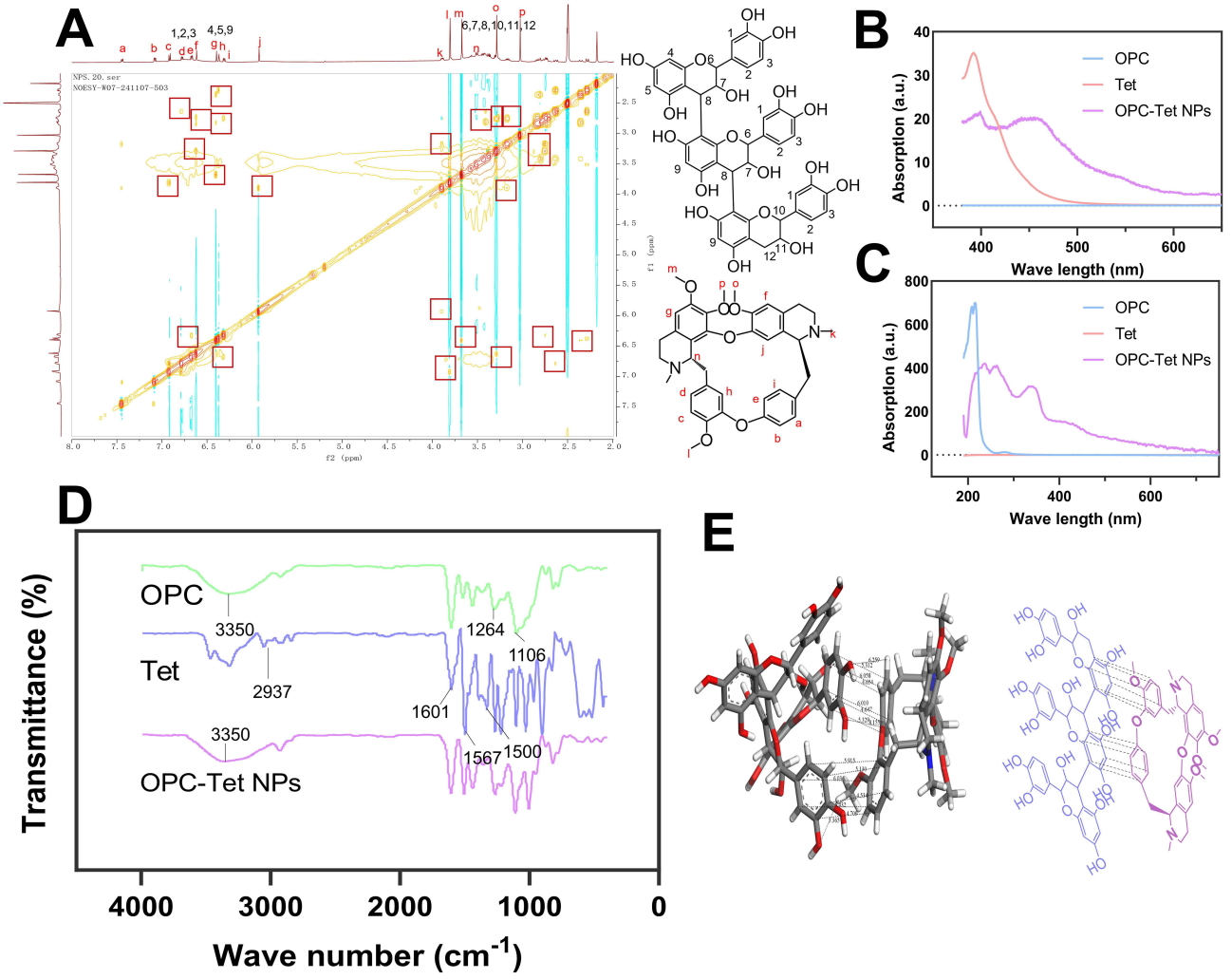

Figure 2 Characterizations of OPC-Tet NPs. (**A**) Schematic diagram of OPC-Tet NPs in 2D-NOESY. The red colored box indicated possible interact sites. (**B**) Fluorescence spectra of OPC, Tet, and OPC-Tet NPs (**C**) UV-vis spectra of OPC, Tet, and OPC-Tet NPs. (**D**) FTIR spectra of OPC, Tet, and OPC-Tet NPs. (**E**) Predicted binding modes of OPC-Tet using MD.

can also observe a large amount of the benzene rings interactions between OPC and Tet. From the results, we can conclude that OPC and Tet could self-assembly and form NPs mainly via π-π interactions.

Biocompatibility

For clinical application, excellent biocompatibility is essential for DDS.[20] The biocompatibility and cytotoxicity of OPC-Tet NPs were evaluated using CCK-8 assay, hemolysis assay, live-dead cell staining, and FCM analysis. As shown in Figure 3A, cell viability remained above 75% when the concentration of OPC-Tet NPs was 40 μg/mL. Hemolysis assays (Figure 3B), conducted by incubating a 2% erythrocyte solution with varying concentrations of OPC-Tet NPs for 3 h, showed minimal erythrocytes hemolysis (< 5%) even at the highest Tet equivalent concentrations of 40 μg/mL. Live-dead staining showed that OPC-Tet NPs did not significantly diminish cell viability, as evidenced by the green and red fluorescence signals in Figure 3C. In the staining experiments, most of the RAW264.7 cells exhibited green fluorescence under various treatments, indicating that OPC-Tet NPs were relatively safe.

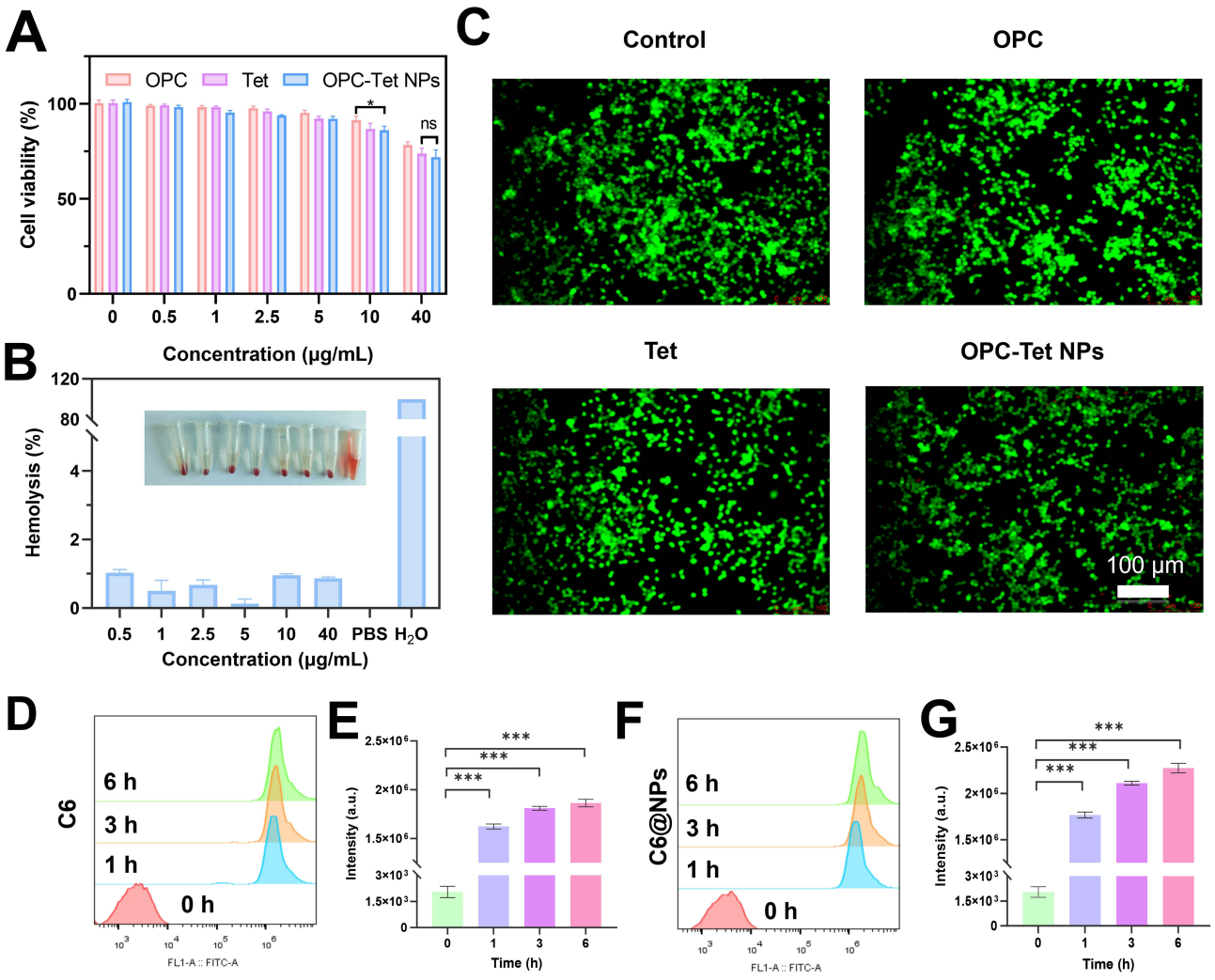

Figure 3 In vitro biocompatibility of OPC-Tet NPs. (**A**) Cell viability of RAW264.7 cells treated with various drug concentrations of OPC, Tet, and OPC-Tet NPs for 24 h. Mean ± SD, n = 3. (**B**) In vitro hemocompatibility assay of different concentrations (0.5, 1, 2.5, 5, 10, 40 μg/mL) of OPC-Tet NPs; (**C**) Representative images of RAW264.7 cells stained with Calcein AM to assess cell viability. (**D**) FCM analysis of C6 uptaked by RAW264.7 cells after 1, 3, and 6-h incubations. (**E**) Quantification of C6 uptake based on FCM data from (D). (**F**) FCM analysis of C6@NPs uptaked by RAW264.7 cells after 1, 3, and 6-h incubations. (**G**) Quantification of C6@NPs uptake based on FCM data from (F). Scale bar: 100 μm; Mean ± SD, n = 3. ns: no significance, $^{*}P < 0.05$, and $^{***}P < 0.001$.

https://doi.org/10.2147/IJN.S531873

Cellular Uptake in vitro

To evaluate the ability of the prepared OPC-Tet NPs to be taken up by cells, we evaluated the cellular uptake of OPC-Tet NPs and analyzed it using FCM. C6 or C6@NPs were incubated with RAW264.7 cells. C6 and C6@NPs showed an increasing trend in fluorescence intensity after 3 h of incubation (Figure 3D–G). FCM results revealed a significant increase in the fluorescence intensity of C6 with the co-assemble of OPC-Tet NPs, suggesting that OPC-Tet NPs enhanced cellular internalization in RAW 264.7 cells.

In vitro Therapeutic Effects

The LPS-induced RAW264.7 cell death after treatment with OPC, Tet, and OPC-Tet NPs was analyzed by FCM. As depicted in Figure 4A, OPC, Tet, and OPC-Tet NPs treatment induced cells death to about 14.2%, 11.2%, and 7.5%, respectively. This indicates that the OPC-Tet NPs showed the ability to inhibit cell death.

OA can trigger oxidative stress responses due to the accumulation of a large amount of ROS.[21,22] ROS and inflammation are not independent entities, instead, they mutually enhance each other. An increase in ROS or pro-inflammatory factors leads to degradation and joint dysfunction. Reducing oxidative stress can alleviate damage of normal tissues and cells.[23,24] ROS generation after LPS treatment was evaluated in Figure 4B. Compared with the LPS

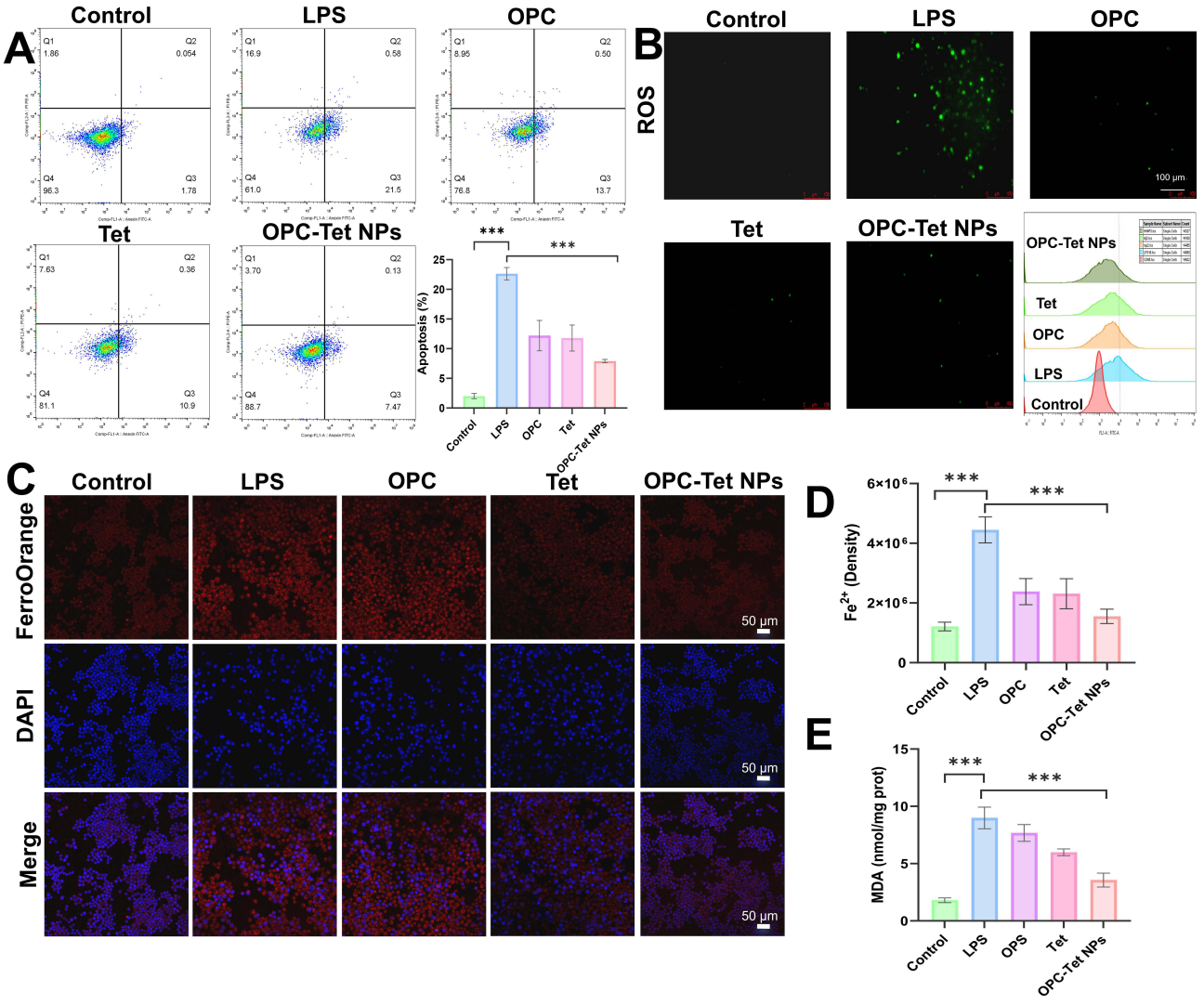

Figure 4 Inhibition of ferroptosis in vitro. (**A**) Apoptosis and quantitative results of RAW264.7 cells in different treatment groups for 24 h. (**B**) The downregulated of ROS production introduced by the presence of OPC, Tet, and OPC-Tet NPs after LPS treatment characterized by FCM. (**C**) Fluorescence images displaying cellular Fe^{2+} (FerroOrange, red; DAPI, blue) after treatment with control, LPS, OPC, Tet, and OPC-Tet NPs. (**D**) Variation in cellular Fe^{2+} concentration in different treatment groups. (**E**) Cellular MDA levels generated by the presence of OPC, Tet, and OPC-Tet NPs after LPS treatment. Scale bar: 100 μm; Scale bar: 50 μm; Mean ± SD, n = 3. ***$P < 0.001$.

group, the ROS levels in the OPC-Tet NPs group were significantly reduced. This demonstrated the superior anti-oxidative stress responses of OPC-Tet NPs compared to OPC and Tet, ameliorating tissue damage and reducing the risk of inflammatory cell infiltration.

ROS and lipid peroxidation play a key role in ferroptosis. MDA is recognized as a marker metabolite of lipid peroxidation. Levels of ROS and MDA can reflect cellular ferroptosis.[25] Cellular Fe^{2+} overload specifically increases ROS and induces membrane lipid peroxidation, leading to cell damage. To verify the effect of OPC-Tet NPs on inhibiting ferroptosis, cells stained with FerroOrange were used to detect intracellular Fe^{2+} (Figure 4C and D). Simultaneously compare MDA levels using an MDA assay kit (Figure 4E). Excessive Fe^{2+} accumulation in the LPS group cells could induce ferroptosis. The Fe^{2+} content decreased after treatment with drugs, especially in OPC-Tet NPs group. Thus OPC-Tet NPs could decrease oxidative stress, restore iron homeostasis, and maintain the cell viability, which shows good therapeutic effect in vitro.

OPC-Tet NPs Release ex vivo

To verify the long-acting release capability of OPC-Tet NPs, the distribution of DIR ex vivo was investigated after intra-articular injection of free DIR and DIR@NPs (Figure S1). Although DIR is continuously absorbed and metabolized, there is still unmetabolized fluorescence in the knee joint, demonstrating the long-acting release capability of OPC-Tet NPs. Even 48 h post-injection, the fluorescence accumulation in mice with DIR@NPs was high than ex vivo, indicating that OPC-Tet NPs can be released for a long time to exert therapeutic effects. On the other hand, the DIR was mainly in joint and had little influence on extra-articular tissues.

Micro-CT

Micro-CT and 3D remodeling revealed that the knee joint of OA mice exhibited sparse trabecular arrangement, suggesting bone loss and surface erosion.[26] OPC, Tet, and OPC-Tet NPs alleviated these injuries to some extent, and the articular surface relatively smooth. In addition, in the groups treated with OPC and Tet, the surface remained rough with evident bone defects (Figure 5A and B). The related quantitative results are detailed in Table S2. Comparison between the control group and OA group showed a decrease in Tb.N, BS/BV, BS/TV, BV/TV, and BMD, indicating considerable bone loss. Similarly, Tb.Sp was also remarkably elevated in the OA joints, indicating the trend of trabecular bone changing from plate-like to rod-like shape.

Compared with the OA group, the levels of BMD and Tb.N in the OPC, Tet, and OPC-Tet NPs groups were significantly higher than those in the OA group; especially the OPC-Tet NPs group, indicating that OPC-Tet NPs had a significant advantage in the treatment of OA by increasing BMD and Tb.N. The widening of the Tb.Sp septum in OA suggested bone loss and corrosion surface of the OA. The narrowing of the Tb.Sp in OA mice after treatment with OPC, Tet, and OPC-Tet NPs suggested that the drug remodeled the trabecular bone by increasing bone mass. Meanwhile, the OPC-Tet NPs group had a remarkable narrowing of Tb.Sp, indicating that the effect of OPC-Tet NPs in the treatment of OA by remodeling trabecular bone was more significant (Figure 5C).

Histopathology Staining

Experimental design was shown in C57BL/6 mice (Figure 6A). The results of H&E staining showed obvious pathological changes in the joints of OA mice (Figure 6B). [27] The cartilage surface of OA mice had severe cartilage erosion. The cartilage surface of mice treated with OPC and Tet was still rough and cracked. The cartilage surface of mice treated with OPC-Tet NPs had a relatively smooth surface, indicating that OPC-Tet NPs significantly prevented the degradation of the extracellular and the destruction of cartilage structure. Currently, the therapeutic effect of OPC-Tet NPs was better than that of OPC and Tet and showed a better performance. In addition, the joint synovia of OA mice were infiltrated by inflammatory cells, part of the extracellular matrix was completely degraded, as indicated by the arrows. Instead, after one month of treatment, OPC-Tet NPs has eliminated the progress of OA and protected cartilage effectively. In OA mice treated with OPC-Tet NPs, the infiltration of inflammatory cells was significantly reduced, demonstrating the advantage of OPC-Tet NPs in their anti-inflammatory effects.

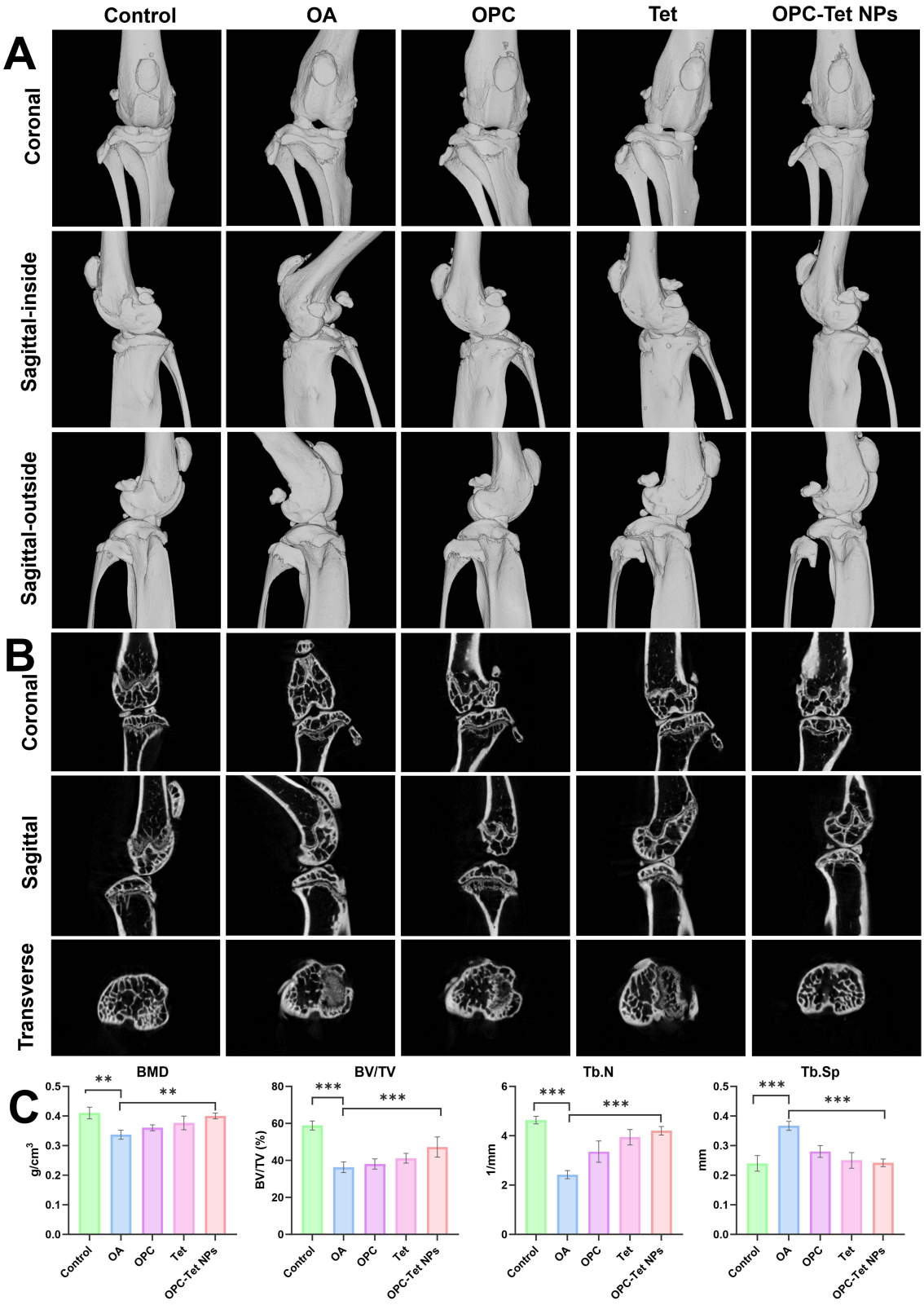

Figure 5 Radiographic evaluation of OPC-Tet NPs for OA treatment. (**A**) The appearance of the tibia, patella, and fibula in different groups after 3D reconstruction of bone morphology in the anteroposterior, medial and lateral positions. (**B**) Micro-CT scans of the coronal, sagittal, and horizontal levels of the right knee joint of mice. (**C**) Quantification of the BMD, BV/TV, Tb.N, and Tb.Sp data collected by micro-CT. Mean ± SD, n = 3. $^{**}P < 0.01$, and $^{***}P < 0.001$.

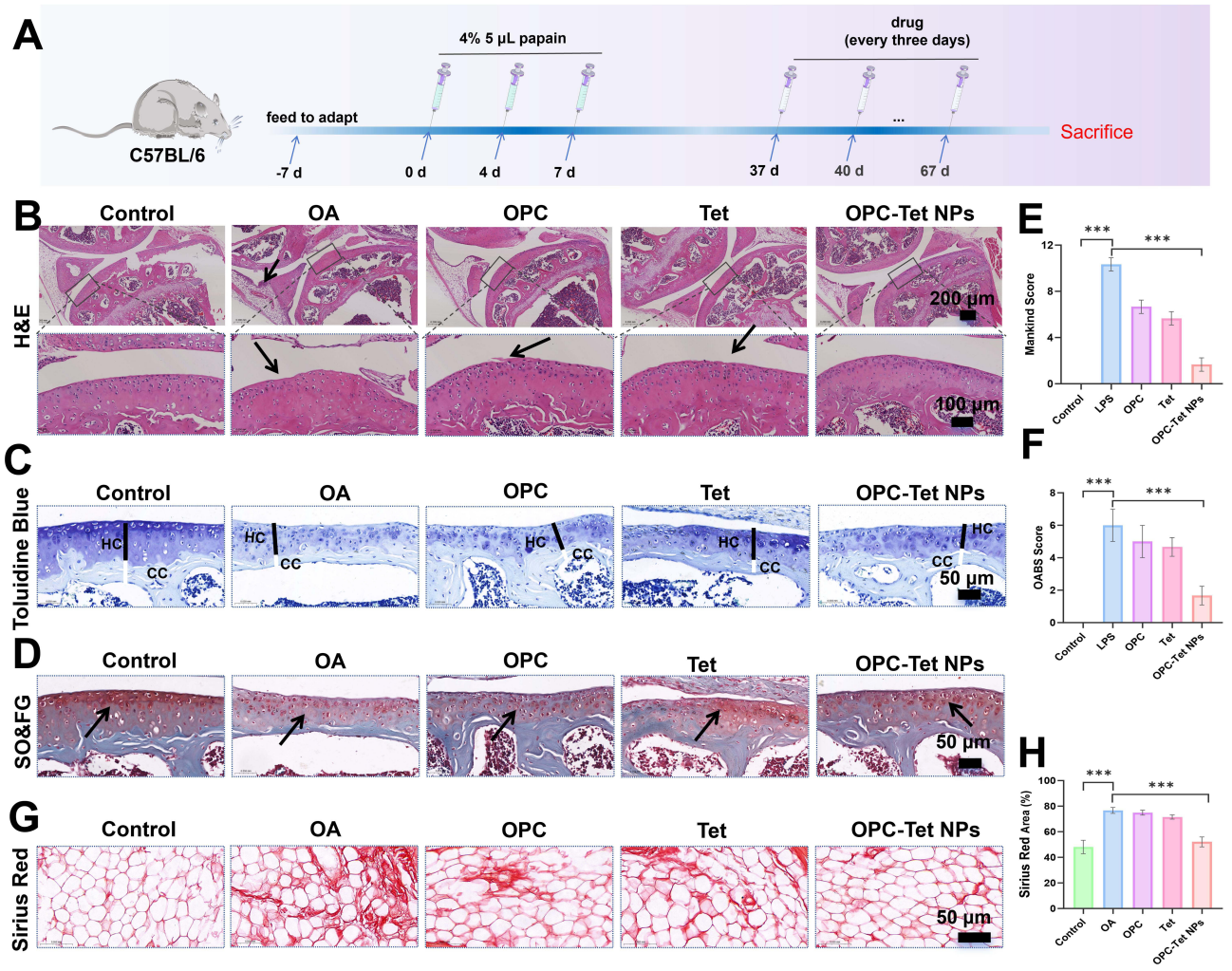

Figure 6 The therapeutic effect of OPC-Tet NPs on histopathology staining. (**A**) Schematic illustration of the experimental design in C57BL/6. (**B**) H&E staining. The black arrows showed that the OA group was infiltrated with synovial inflammatory cells, the cartilage surface is rough, and the chondrocytes were disordered. The surface of the OPC group is rough. The surface of the Tet group was rough and cracked. The zoomed-in area was marked as a black box. The arrow indicated abnormal organization state. Scale bar: 200 μm and 100 μm. (**C**) Toluidine Blue staining. The OA group and OPC group shown by the arrow had a shallower tide line than the control group. The black light is HC, and white is CC. Scale bar: 50 μm. (**D**) SO&FG staining. In the control group, OA group, and OPC-Tet NPs group, the proteoglycans by the black arrows was stained dark red, with the OA group showing a noticeable light color. Scale bar: 50 μm. (**E**) The Mankin score evaluated the result of OA cartilage histopathology. (**F**) The OABS score evaluated the result of OA cartilage histopathology. Scale bar: 50 μm. (**G**) Sirius Red staining. Images of mice knee joint tissues with OA. (**H**) The analysis data with Sirius Red. Mean ± SD, n = 3. $^{**}P < 0.01$, $^{***}P < 0.001$.

To further observe the cartilage in OA mice after different treatments, Toluidine Blue staining was used (Figure 6C). The tidal line between hyaline cartilage (HC) and calcified cartilage (CC) in the control group was intact, and the cells were neatly arranged.[28] However, interrupted tidal lines, fuzzy edges, and decreasing of the CC layer can be observed in OA mice, suggesting that intra-articular injection of papain alters the tidal structure of mice cartilage. OPC, Tet, and OPC-Tet NPs all alleviated the damage, especially in the OPC-Tet NPs group. After treatment with OPC-Tet NPs, the tide line had a relatively clear surface, and the cartilage was remarkably thickened.

SO&FG staining was used to evaluate the loss of proteoglycan in the cartilage. The proteoglycan of articular cartilage assessed by safranin-O staining is presented in red, and bone tissue assessed by solid green is presented blue-green. The number of proteoglycans in articular cartilage in the OA mice group decreased, and the number of chondrocytes in mice increased after OPC, Tet, and OPC-Tet NPs treatments. It should be noted that the increase of OPC-Tet NPs was remarkable as shown in Figure 6D.

Using various histological staining methods, we evaluated the effectiveness of OPC-Tet NPs in treating OA. Both the Mankin score and OABS score systems indicated an advantage of OPC-Tet NPs in OA treatment.[29,30] The quantitively of

https://doi.org/10.2147/IJN.S531873

Mankin score and OABS score shown in Figure 6E and F, demonstrating the remarkable advantages of OPC-Tet NPs in the treatment of OA.

In OA, chronic inflammation can lead to synovial fibrosis. Using Sirius Red staining, we observed that some areas in the synovial tissue of OA mice were deeply stained, indicating a high degree of fibrosis. Quantifying the fibrotic regions in the synovial tissue (Figure 6G and H) revealed that OPC-Tet NPs effectively reduced synovial fibrosis, further confirming the advantages of OPC-Tet NPs in managing OA.[31]

Based on the results, we can find that the as-prepared OPC-Tet NPs showed prolonged release compared to free DIR after intra-articular injection. However, due to antioxidant activity of OPC, the system could collapse and tend to influence local lesion in short time. The frequency of administration is also a disadvantage to clinical translation. The stoichiometric composition of OPC-Tet NPs should be further explored to realize the maximized output-to-input ratio. The method of drug administration should also be improved. The progress to clinical applicability should be more experts from various fields collaborating to advance.

IHC

OA is considered a chronic inflammatory disease involving the entire joint. In OA, the expression of pro-inflammatory factors IL-6 and TNF-α in vascular endothelial cells increases, and part of the synovial tissue is infiltrated by inflammatory cells.[32,33] Uncontrolled pro-inflammatory factors can lead to cell death within the joints, which is due to the inflammatory response and the excessive release of inflammatory factors. Long-term infiltration of inflammatory factors can lead to the continuous destruction of cells in the joints, and prompt drug treatment is crucial. OPC and Tet have been recognized to have good anti-inflammatory effects, and the anti-inflammatory potential of OPC-Tet NPs needs to be verified. IHC and IF were used to evaluate the anti-inflammatory effects of NPs.

IL-6 and TNF-α were quantitatively detected by IHC, shown in Figure 7A. The expression of IL-6 and TNF-α in the knee joint sections was stained yellowish-brown. To further verify the anti-inflammatory effect of OPC-Tet NPs, IF staining for IL-6 and TNF-α was performed on pathological sections (Figure 7B), and the quantitative results were consistent with those obtained by IHC. The anti-inflammatory effects of OPC-Tet NPs have been demonstrated.

The results showed that the levels of IL-6 and TNF-α in the knee joint of OA mice were higher than those in the control group ($P < 0.05$), and the levels of IL-6 and TNF-α were reduced after treatment with OPC, Tet, and OPC-Tet NPs, especially in OPC-Tet NPs group (Figure 7C), suggesting that OPC-Tet NPs could down-regulated the expression of IL-6 and TNF-α to manage OA.

The Mechanism of Anti-Ferroptosis

Ferroptosis is an iron-dependent cell death featured by accumulation of lipid peroxidation. To further verify the effect of OPC-Tet NPs on Fe^{2+} overload, we used IHC to analyze the key proteins ACSL4 and GPX4.[34–36] When ACSL4 is activated, polyunsaturated fatty acid (PUFA) and phospholipids are peroxidized under ROS stimulation, leading to cell membrane destruction and ferroptosis. When GPX4 activity is inhibited, lipid peroxides cannot be efficiently metabolized by the GPX4-catalyzed glutathione reductase reaction, and the accumulation of Fe^{2+} catalyzes the production of ROS, further exacerbating cell membrane destruction and ferroptosis.

To explore the effect of OPC-Tet NPs on ferroptosis, the expression levels of ACSL4 and GPX4 were evaluated by IHC. The results showed that compared with the control group, the expression levels of ACSL4 protein in the OA group were increased and the protein expression levels of GPX4 decreased. Compared with the OA group, the expression levels of ACSL4 protein decreased ($P < 0.001$), and the expression levels of GPX4 protein in the OPC-Tet NPs group increased ($P < 0.001$). These results suggest that OPC-Tet NPs inhibit ferroptosis by decreasing intracellular ACSL4 and upregulating GPX4, thereby reducing the content of intracellular lipid peroxidation substrates. This verified the advantage of OPC-Tet NPs in anti-ferroptosis.

The results of TUNEL staining (Figure 7D) showed that OPC-Tet NPs could inhibit cell death through inflammatory and ferroptosis mechanisms, and the effect was better than that of OPC or Tet alone. The quantification of GPX4, ACSL4 and TUNEL on IHC were shown in Figure 7E.

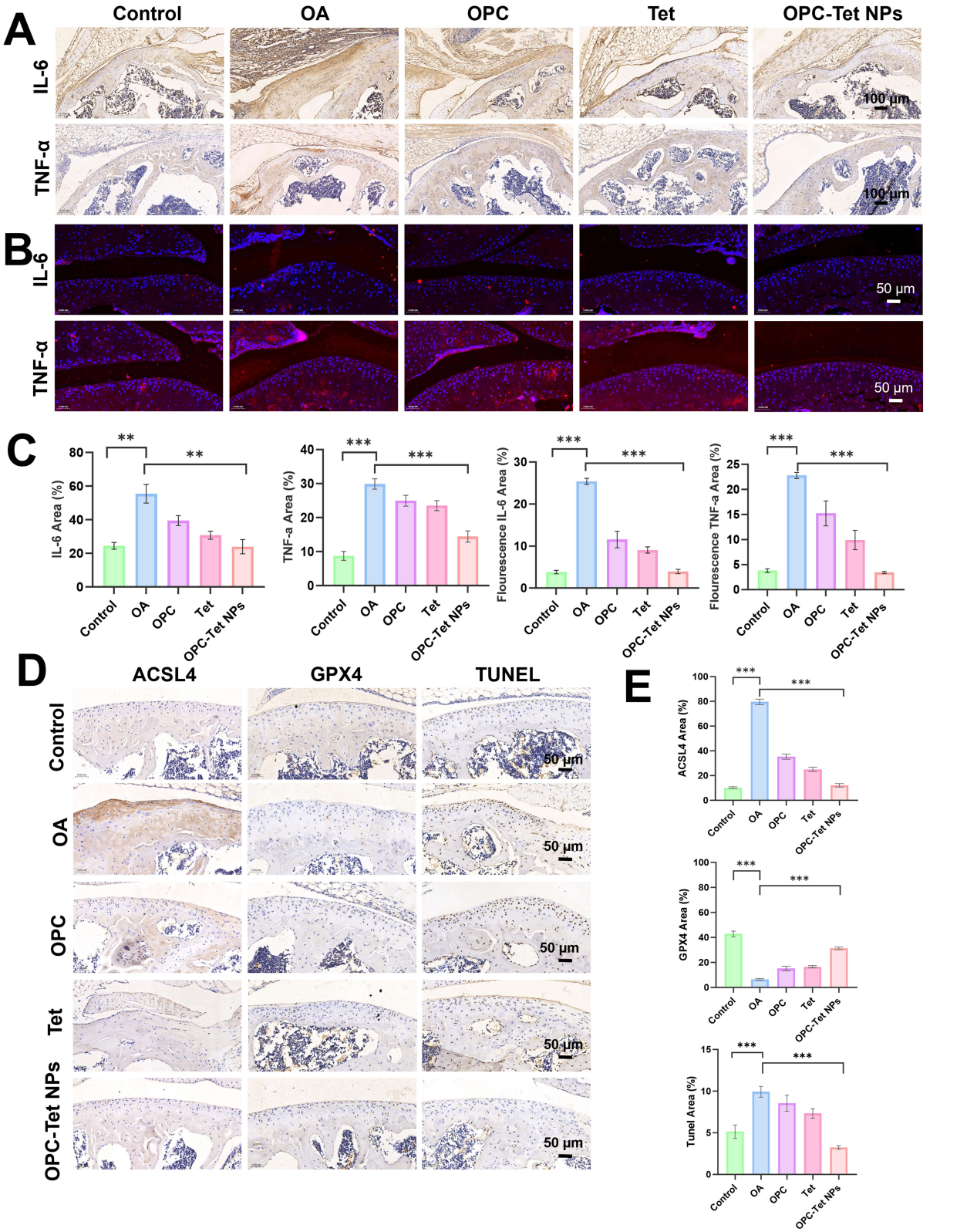

Figure 7 Mechanism of action of OPC-Tet NPs in the treatment of OA in mice. (**A**) Images of IHC staining of IL-6 and TNF-α. Scale bar: 100 μm. (**B**) Images of IF staining of IL-6 and TNF-α. Scale bar: 50 μm. (**C**) The quantification of IL-6, TNF-α on IHC and IF images. (**D**) IHC images of GPX4, ACSL4 and TUNEL. Scale bar: 50 μm. (**E**) The quantification of GPX4, ACSL4, and TUNEL on IHC. Mean ± SD, n = 3. $^{**}P < 0.01$, and $^{***}P < 0.001$.

https://doi.org/10.2147/IJN.S531873

Conclusion

Based on the non-covalent self-assembly between OPC and Tet, a novel OPC-based NPs to manage OA was proposed. The OPC-Tet NPs exhibited good biocompatibility and sustained release capabilities. After a month of administration, the joints showed eliminated 10.5% BMD score compared to Tet group according to micro-CT. Sirius red staining results demonstrated 23.6% decreased fibrosis of OPC-Tet NPs compared to Tet group. Moreover, OPC-Tet NPs could regulate key proteins involved in inflammation and ferroptosis, effectively alleviating intra-articular inflammation and protecting cartilage from damage.

However, small sample size and the absence of standard drug comparisons are two limitations and may affect the generalizability of the results. Dose optimization and pharmacokinetic profiling remain to be established for future translational application. Further research should focus on chronic OA and aged OA models. In summary, the self-assembly of OPC and Tet offers a new strategy for OA management. Based on the long history of these natural molecules in Chinese medicine, safety profiles of OPC and Tet have been widely verified. This strategy possesses great clinical potential.

Data Sharing Statement

Data will be made available on request from the corresponding authors.

Funding

This work was supported by Shenzhen Fundamental Research Program (Grant number JCYJ20220530144802005), Research Excellence Program of Chengdu Sport University (Grant number 2025-A002), Scientific Research Start-up Foundation of Chengdu Sport University (Grant number 2023cdtyky05), General Project of Sichuan Natural Science Foundation for Science and Education Joint Fund (Grant number 2025NSFSC2102).

Disclosure

The authors declare no conflicts of interest in this work.

References

1. Wang S, Li W, Zhang P, et al. Mechanical overloading induces GPX4-regulated chondrocyte ferroptosis in osteoarthritis via piezo1 channel facilitated calcium influx. *J Adv Res*. 2022;41:63–75. doi:10.1016/j.jare.2022.01.004
2. Al-Hetty HRAK, Abdulameer SJ, Alghazali MW, et al. The role of ferroptosis in the pathogenesis of osteoarthritis. *J Membrane Biol*. 2023;256:223–228. doi:10.1007/s00232-023-00282-0
3. Hu Z, Chen L, Zhao J, et al. Lipoxin A4 ameliorates knee osteoarthritis progression in rats by antagonizing ferroptosis through activation of the ESR2/LPAR3/Nrf2 axis in synovial fibroblast-like synoviocytes. *Redox Biol*. 2024;73:103143. doi:10.1016/j.redox.2024.103143
4. Fan X, Sun AR, Young RSE, et al. Spatial analysis of the osteoarthritis microenvironment: techniques, insights, and applications. *Bone Res*. 2024;12:7. doi:10.1038/s41413-023-00304-6
5. Bindu S, Mazumder S, Bandyopadhyay U. Non-steroidal Anti-inflammatory Drugs (NSAIDs) and organ damage: a current perspective. *Biochem Pharmacol*. 2020;180:114147. doi:10.1016/j.bcp.2020.114147
6. Zouka YE, Sheta E, Salama MA, et al. Tetrandrine ameliorated atherosclerosis in vitamin D3/high cholesterol diet-challenged rats via modulation of MiR-34a and Wnt5a/Ror2/ABCA1/NF-kB trajectory. *Sci Rep*. 2024;14(1):21371. doi:10.1038/s41598-024-70872-y
7. Zhang S, Zhan J, Li M, et al. Therapeutic potential of traditional Chinese medicine against osteoarthritis: targeting the Wnt signaling pathway. *Am J Chinese Med*. 2024;52(07):2021–2052. doi:10.1142/S0192415X24500782
8. Liu Y, Zhao YQ, Wang LP, et al. Preparation and characterization of tetrandrine-phospholipid complex loaded lipid nanocapsules as potential oral carriers. *Int J Nanomed*. 2013;8:4169–4181. doi:10.2147/IJN.S50557
9. Xin L, Ning S, Wang H, et al. Tumor microenvironment responsive and platelet membrane coated polydopamine nanoparticles for cancer radiosensitization by inducing cuproptosis. *Int J Nanomed*. 2025;20:3643–3652. doi:10.2147/IJN.S504148
10. Tian X, Wang P, Li T, et al. Self-assembled natural phytochemicals for synergistically antibacterial application from the enlightenment of traditional chinese medicine combination. *Acta Pharm Sin B*. 2020;10(9):1784–1795. doi:10.1016/j.apsb.2019.12.014
11. Chaurasiya M, Kumar G, Paul S, et al. Natural product-loaded lipid-based nanocarriers for skin cancer treatment: an overview. *Life Sci*. 2024;357:123043. doi:10.1016/j.lfs.2024.123043
12. Xu G, Ma C, Chu H, et al. Anti-inflammatory combination of puerarin and Ac2-26 using intranasal delivery for effective against ischemic stroke in rat model. *Int J Nanomed*. 2025;20:3825–3842. doi:10.2147/IJN.S508800
13. Liu J, Li K, Li S, et al. Grape seed-derived procyanidin inhibits glyphosate-induced hepatocyte ferroptosis via enhancing crosstalk between Nrf2 and FGF12. *Phytomedicine*. 2024;123:155278. doi:10.1016/j.phymed.2023.155278
14. Huang Y, Wang X, Chen H, et al. Self-assembly oligomeric anthocyanin-based core–shell structure of nanoparticles enhances the delivery and efficacy of berberine in osteoarthritis. *ACS Biomater Sci Eng*. 2025;11(5):2739–2752. doi:10.1021/acsbiomaterials.5c00037
15. Yao Y, Xu Z, Ding H, et al. Carrier-free nanoparticles-new strategy of improving druggability of natural products. *J Nanobiotechnology*. 2025;23(1):108. doi:10.1186/s12951-025-03146-y

16. Wójcik-Pastuszka D, Anna F, Witold M. Influence of the acceptor fluid on the bupivacaine release from the prospective intra-articular methylcellulose hydrogel. *Pharmaceutics*. 2024;16(7):867. doi:10.3390/pharmaceutics16070867
17. Xing C, Sheng Y, Wu Y, et al. Carrier-free small molecule-assembled nanoparticles for treatment of sepsis. *ACS Appl Nano Mater*. 2024;7 (20):24049–24060. doi:10.1021/acsanm.4c04630
18. Liow SS, Zhou H, Sugiarto S, et al. Highly efficient supramolecular aggregation-induced emission-active pseudorotaxane luminogen for functional bioimaging. *Biomacromolecules*. 2017;18(3):886–897. doi:10.1021/acs.biomac.6b01777
19. Yu X, Liang T, Wang M, et al. An innovative extraction strategy for herbal medicine by adopting P-sulphonatocalix [6]/[8]arenes. *Phytochem Anal*. 2022;33(7):1068–1085. doi:10.1002/pca.3160
20. Cai X, Xie Z, Ding B, et al. Monodispersed Copper(I)-based nano metal–organic framework as a biodegradable drug carrier with enhanced photodynamic therapy efficacy. *Adv Sci*. 2019;6(15):1900848. doi:10.1002/advs.201900848
21. Xing C, Chen H, Guan Y, et al. Cyclodextrin-based supramolecular nanoparticles break the redox balance in chemodynamic therapy-enhanced chemotherapy. *J Colloid Interface Sci*. 2022;628:864–876. doi:10.1016/j.jcis.2022.08.110
22. Chen H, Xing C, Lei H, et al. ROS-driven supramolecular nanoparticles exhibiting efficient drug delivery for chemo/chemodynamic combination therapy for cancer treatment. *J Control Release*. 2024;368:637–649. doi:10.1016/j.jconrel.2024.03.015
23. Lepetsos P, Papavassiliou AG. ROS/oxidative Stress Signaling in Osteoarthritis. *Biochim Biophys Acta Mol Basis Dis*. 2016;1862(4):576–591. doi:10.1016/j.bbadis.2016.01.003
24. Zhang S, Wang L, Kang Y, et al. Nanomaterial-based reactive oxygen species scavengers for osteoarthritis therapy. *Acta Biomater*. 2023;162:1–19. doi:10.1016/j.actbio.2023.03.030
25. Zhang X, Hou L, Guo Z, et al. Lipid peroxidation in osteoarthritis: focusing on 4-hydroxynonenal, malondialdehyde, and ferroptosis. *Cell Death Discov*. 2023;9(1):1–13. doi:10.1038/s41420-023-01613-9
26. Oláh T, Walter F, Pape D, et al. Quantitative subchondral bone microstructural changes detect knee osteoarthritis in patients by in vivo clinical computed tomography. *Osteoarthr Cartil*. 2022;30:S290–S291. doi:10.1016/j.joca.2022.02.389
27. McNulty MA, Loeser RF, Davey C, et al. Histopathology of naturally occurring and surgically induced osteoarthritis in mice. *Osteoarthr Cartil*. 2012;20(8):949–956. doi:10.1016/j.joca.2012.05.001
28. Li Q, Xu JY, Hu X, et al. The protective effects and mechanism of ruyi zhenbao pill, a tibetan medicinal compound, in a rat model of osteoarthritis. *J Ethnopharmacol*. 2023;308:116255. doi:10.1016/j.jep.2023.116255
29. Koushesh S, Shahtaheri SM, McWilliams DF, et al. The Osteoarthritis Bone Score (OABS): a new histological scoring system for the characterisation of bone marrow lesions in osteoarthritis. *Osteoarthr Cartil*. 2022;30(5):746–755. doi:10.1016/j.joca.2022.01.008
30. Busa P, Lee SO, Huang N, et al. Carnosine alleviates knee osteoarthritis and promotes synoviocyte protection via activating the Nrf2/HO-1 signaling pathway: an in-vivo and in-vitro study. *Antioxidants*. 2022;11(6):1209. doi:10.3390/antiox11061209
31. Zhang L, Xing R, Huang Z, et al. Inhibition of synovial macrophage pyroptosis alleviates synovitis and fibrosis in knee osteoarthritis. *Mediators of Inflamm*. 2019;2019(1):2165918. doi:10.1155/2019/2165918
32. Koyama T, Uchida K, Fukushima K, et al. Elevated levels of TNF-α, IL-1β and IL-6 in the synovial tissue of patients with labraltear: a comparative study with hip osteoarthritis. *BMC Musculoskelet Disord*. 2021;22(1):33. doi:10.1186/s12891-020-03888-w
33. Cook AD, Lee MC, Saleh R, et al. TNF and granulocyte macrophage-colony stimulating factor interdependence mediates inflammation via CCL17. *JCI Insight*. 2018;3(6):e99249. doi:10.1172/jci.insight.99249
34. Lai W, Huang R, Wang B, et al. Novel aspect of neprilysin in kidney fibrosis via ACSL4-mediated ferroptosis of tubular epithelial cells. *MedComm*. 2023;4:e330. doi:10.1002/mco2.330
35. Tay CY, Fan W, Setyawati MI, et al. Nano-hydroxyapatite and nano-titanium dioxide exhibit different subcellular distribution and apoptotic profile in human oral epithelium. *ACS Appl Nano Mater*. 2014;6(9):6248–6256. doi:10.1021/am501266a
36. Yao X, Sun K, Yu S, et al. Chondrocyte ferroptosis contribute to the progression of osteoarthritis. *J Orthop Translat*. 2021;27:33–43. doi:10.1016/j.jot.2020.09.00